Research Article | Vol. 30, No. 13 / 20 Jun 2022 / Optics Express 22679
Optics EXPRESS

Visible and short-wavelength infrared light collimation through carbon nanotube, parallel-hole collimators

TYLER WESTOVER,[1,2,*] SCOTT OLSEN,[1] ZACH WESTHOFF,[1] NICK MORRILL,[2] ROBERT DAVIS,[1] AND RICHARD VANFLEET[1]

[1]Brigham Young University Department of Physics and Astronomy, N283 ESC, Provo, Utah 84602, USA
[2]Tula Health Inc., 686 N Arbinger Way, Farmington, Utah 84025, USA
[*]tyler.westover13@gmail.com

Abstract: Traditional collimators typically require large optics and/or long pathlengths which makes miniaturization difficult. Carbon nanotube templated microfabrication offers a solution to pattern small 3D structures, such as parallel hole collimators. Here we present the characterization of a carbon nanotube parallel hole collimator design and its efficacy in visible and short wavelength infrared light. Comparison to geometric and far field diffraction models are shown to give a close fit, making this a promising technology for miniaturized diffuse light collimation.

1. Introduction

In many optical detection applications, the light of interest becomes diffuse after passing through a sample and requires some form of collimation for analysis; unfortunately, traditional collimators using lenses or multiple apertures are difficult to shrink, presenting a roadblock to the miniaturization of optical systems. However, parallel-hole collimators show promise for optical collimation and are amenable to miniaturization by using small, closely-spaced holes in a relatively thin plate. When the spacing between holes is small, a sidewall material with high absorption is required for effective collimation. Previously miniaturized parallel-hole collimators have been fabricated using silicon micromachining to analyze visible light from highly scattering media [1,2].

Carbon composite, parallel-hole collimators formed using carbon nanotube templated microfabrication (CNT-M) offer several potential advantages over silicon-based alternatives. These advantages include the facility of precise, high-aspect-ratio fabrication [3,4] as well as the highly absorptive nature of carbon composites in both visible and—unlike silicon—infrared wavelengths of light. Patterned, vertically-aligned CNTs are extremely fragile, making them difficult to handle in processing and severely limiting the range of applications. However, CNT-M uses carbon infiltration (or other infiltration materials) to significantly improve the robustness of high-aspect-ratio CNT structures [5–8] while retaining the high-fidelity patterning. The pyrolytic carbon infiltration process deposits carbon onto the surface of individual CNTs, effectively thickening them and bonding them together. After carbon infiltration, optical imaging shows that these structures are still very absorptive [9].

In this work we used carbon-infiltrated CNT-M to form parallel hole collimators for use in the visible and near-infrared. The patterned CNTs were formed into a rectangular grid with pore sizes of 25, 50, 100 and 200 microns and heights between 100 and 880 microns. Collimation performance was determined by measuring transmission through the micro-collimators as a function of angle. Briefly, collimated light (both visible and NIR sources) was passed through the CNT micro-collimators and transmitted light was detected using either silicon or InGaAs photodetector. The collimator was tilted through various angles; at each angle the intensity at the detector was recorded. The reduction in intensity through various angles was modeled using both

#458656 https://doi.org/10.1364/OE.458656
Journal © 2022 Received 29 Mar 2022; revised 19 May 2022; accepted 23 May 2022; published 7 Jun 2022

Optics EXPRESS

a basic geometric approach and one incorporating far-field diffraction effects. We have verified that CNT-M collimators perform very closely to the predicted values as modeled. The aspect ratios (collimator height divided by pore width) ranged from 1.25 to 32 with cutoff halfwidth angles (angle at which no light passes through) ranging from 3 to 38 degrees. We have also verified through modeling that some single sidewall scattering occurs and measured a detectable amount of double sidewall scattering.

2. Methods

CNT-M fabrication was performed as described by Fazio et al. [9]. Briefly, CNT growth substrates were prepared by sputtering 50-70 nm of alumina on single-crystal silicon wafers (Fig. 1(A)). Patterned thin film iron catalyst was then added as follows (Fig. 1(B)). Photoresist (AZ3330, AZ Electronic Materials) was spun onto the wafers at 5000 rpm. The collimator pattern was exposed with UV light for 10 seconds. The photoresist was then developed in AZ300MIF (AZ Electronic Materials) for 45 seconds. Excess photoresist was removed by a 30 second water rinse. The wafer was then dried using a nitrogen gun. Using a thermal evaporator, 4 nm of iron was deposited onto the patterned photoresist. Liftoff of the excess iron was done by sonication of the sample in 1-methyl-2-pyrrolidone, (Sigma Aldrich) for 5 minutes. Samples were then rinsed in deionized water and dried using nitrogen. CNT growth was accomplished in a 1 inch quartz tube furnace at 750 °C. Hydrogen and ethylene were introduced at flow rates of 311 sccm and 338 sccm, respectively. Growth times varied from 2-15 minutes depending on the target growth height, after which the ethylene flow was turned off and the temperature increased to 900 °C for carbon infiltration of the CNT forest. Once the target temperature was reached, ethylene flow was reintroduced at 338 sccm for 10 minutes (Fig. 1(C)). The tube was then cooled in argon. The sample was then removed, followed by a plasma etch (Techinics Planar Etch 2) in an oxygen plasma at 200 W in 5 minute intervals to remove the floor layer (a layer of carbon on the substrate and bottom of the CNT forest formed during infiltration). After each 5 minute interval, the chamber was vented, and the forest inspected. Once, CNT forest had separated from the silicon substrate, the forest was flipped over, exposing the bottom, and an additional 5 minute, 200 W plasma clean was performed (Fig. 1(D)).

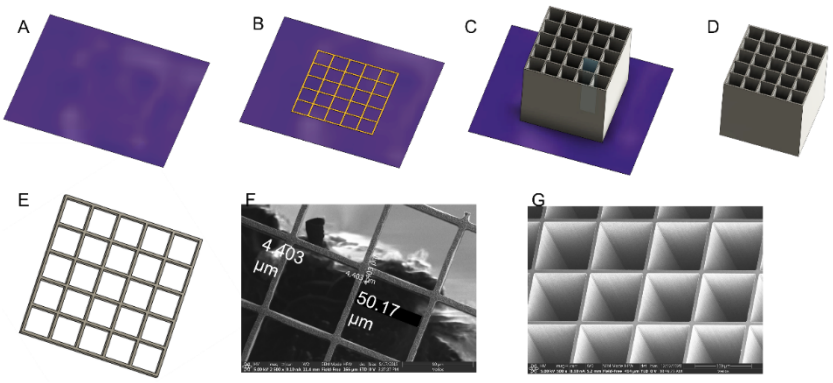

Fig. 1. CNT growth process. A) Alumina is deposited on single crystal silicon substrate B) 4nm of iron is photolithographically patterned onto the substrate C) Patterned CNTs are grown and D) CNT-M collimator is released from the substrate using plasma etch. E) Top down view of the collimator showing the square pores and the open channel. F) SEM image of the top view of the collimator showing the tops of the walls and the open channel. G) Angled SEM image of a collimator showing the walls and square channel.

Optics EXPRESS

Sample heights were measured using an optical microscope (Olympus BX60, Olympus UMPlanFl 20x lens). Focusing on the top and the bottom of the CNT forest allowed for the determination of height with the stage height dial; this method for height measurements has an approximate error of 10-20 µm as compared to a calibrated SEM measurements on the same sample. To minimize errors due to backlash in the optical microscope mechanical stage, measurements were performed moving only downward until the top of the collimator is in focus, pausing to record the position at the top, then continuing only downward until the bottom of the collimator is in focus and the bottom position is recorded. To verify heights and determine lateral dimensions of the pore size and wall thickness, a few collimators were characterized by scanning electron microscopy using a Verios G4 SEM.

The infiltrated CNT collimators were mounted onto 33 mm OD, 13 mm ID washers using gel superglue on the corners for optical testing. The washer was then inserted into an optical mount on a rotation stage. The optical test setup is diagramed in Fig. 2. A laser at the source position was used for alignment of optical elements: lens, aperture, collimator, and detector. LEDs of desired wavelengths (red - 650 nm or IR - 1550 nm) were used. The light from the LED was collimated by adjusting the distance between the LED and the lens (focal length 50 mm, diameter 25 mm). The aperture was adjustable and set to a 1 mm opening for 660 nm and 1 cm opening for 1550 nm. The distance between the CNT collimator and the photodetector (Si with 4.4 mm x 4.4 mm effective area, InGaAs with 1 mm x 1 mm effective area) was ~125 mm. The collimation of the beam was determined using a setup containing only the LED and the lens, by measuring the beam size at the lens (25 mm diameter beam) exit and again at 60 cm past the lens. There was no more than a ~2 mm change in beam size over the 60 cm distance giving a collimation of ~0.3 degrees. The beam reference intensity was recorded with the collimator removed and a dark level was recorded with the beam blocked. Zero tilt incidence, in reference to the LED, was found by rotating the collimator until the maximum intensity was recorded on the detector. As the collimator is tilted, the reduction in intensity is due to the size of the direct optical path being decreased, until it is completely cut off, represented schematically in Figs. 2(B)-(D). The intensity of the light at the photodetector was recorded at varying angles.

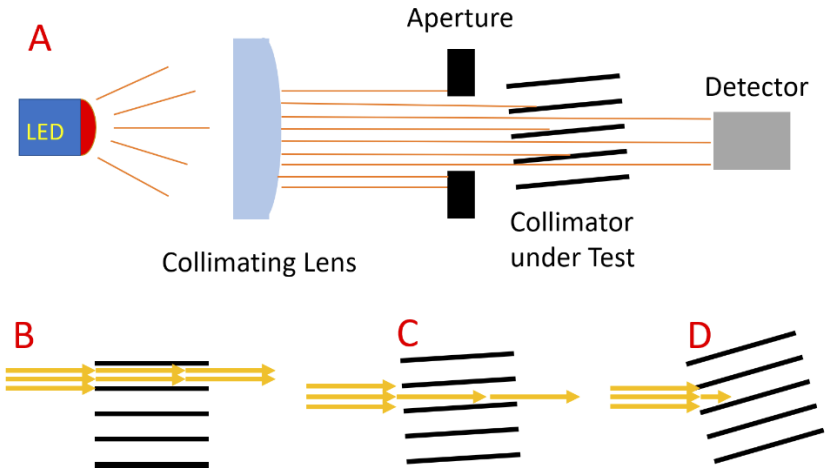

Fig. 2. Illustration of the optical test setup and process. A) A LED was collimated using a lens and an aperture, which then passed through a collimator and was collected at the detector B) A large portion of the light passes through when it is perpendicular to the collimator surface C) As the collimator is tilted light is partially blocked illustrating the reduced transmission off-angle light D) As the angle is increased beyond a cut-off point, there is no straight path for light through the collimator.

Optics EXPRESS

The above experimental description includes variation and measurement of only one tilt axis. The collimator is a 2-dimensional array with a degree of alignment determined by two tilt axis angles. The second tilt axis and rotation about the beam direction were not explicitly varied. While mounting the collimator on the washer, and the washer in the optical mount, effort was made to align the second tilt axis and to align the array directions with the tilt axes. Any offset in the second tilt direction will decrease the peak transmission, but subsequent tilt variation of the primary tilt direction should still be linear.

Collimators with pore sizes of 25, 50, 100 and 200 microns were studied. The collimators were grown to varying heights ranging from 100 to 880 microns to test various aspect ratios. In this work the aspect ratio is defined as the height of the collimator divided by the pore size (h/d). Red (650 nm) and IR (1550 nm) LEDs were used to illustrate the visible and IR ranges. For red light the detector was 4.4 mm x 4.4 mm for IR sources, the available detectors are small (1 mm x 1 mm) and an integrating sphere with an 11.2 mm diameter entrance size was used to collect more light, increasing our signal to noise. The location of the collection port of the sphere reduced the optical pathlength from 125 mm to 90 mm.

3. Results and discussion

Optical transmission measurements were measured for collimators with square pores with dimensions of $25 \times 25\,\mu m$, $50 \times 50\,\mu m$, $100 \times 100\,\mu m$ and $200 \times 200\,\mu m$. Transmission was measured for angles ranging from normal incidence to well beyond the cut off angle of each collimator as illustrated in Figs. 2(B)-(D). Applying a strictly geometric model, the intensity of the light should decrease linearly as the collimator is tilted toward the optical axis ($I = I_o(1 - \frac{h}{d}\tan(\theta))$). The angle at which the light is completely cut off is then the Arctangent of the pore size divided by the height of the collimator, i.e. the $\tan^{-1}\left(\frac{d}{h}\right)$. Figure 3 shows measured transmission data and model calculations using 650 nm light for a representative low aspect ratio (Fig. 3(A)) and high-aspect-ratio (Fig. 3(B)) collimator as well as the measured and modeled cutoff angle vs aspect ratio (Fig. 3(C)) (Dataset 1 (Ref. [10])). The model curves in Figs. 3(A) and 3(B) are not fits to the data but were calculated using measured properties such as height, pore size, beam width and detector size (Code 1 (Ref. [11])). In addition to the 10-20 µm uncertainty in the height measurement, there is a variance in height across the sample that can be as much as 10-15% of the height. Allowing some error in these geometric quantities, the simple geometric model has a reasonable match to the data. However, transmission measurements for the lower aspect ratio collimator (1.25 ratio for Fig. 3(A)) were found to decrease with tilt faster than the 250 µm tall model would predict, but matches a 275 µm tall collimator shown in the green dotted line. The 275 µm height falls within the height measurement uncertainty in these samples. The addition of far field diffraction to the model slightly decreases the transmission at larger incident angles, although this change is small compared to the impact of height uncertainty A far field diffraction model was used due to the distance between the collimator and the detector (9-12.5 cm) being large compared to the wavelength. The model is based on an array of simple slits that decreases in projected width with tilt, assuming total absorption by the sidewalls. In this model, the diffraction effects broaden the distribution at the detector sending intensity beyond the detector edges. Higher order diffraction peaks extending past the edge of the detector can be seen by eye, supporting the model premise (Supplementary Visualization 1). The largest effect would be seen if only the main transmission peak was included in the detector. The detector size includes most of the diffraction peaks, making the diffraction correction relatively small. However, the lower transmission at high tilt angles will become more prominent for low aspect ratio collimators and at larger collimator to detector separations due to the decreasing effective slit width placing more intensity beyond the detector. This effect is much smaller in higher aspect ratio collimators due to fewer datapoints in the tilt range and is also minimal in the IR

Optics EXPRESS

data due to the detector size collecting more diffraction peaks than in the visible. At non-normal incidence some shallow angle light will be reflected off the sidewalls and hit the detector due the detectors size and proximity to the collimator. Light reflected off a single wall may contribute to the detected signal but, must have an angle less than ~2 degrees (~7 degrees) to hit the detector for 660 nm (1550 nm). Both geometric and diffraction corrected models were used to predict transmission only up to the cut off angle.

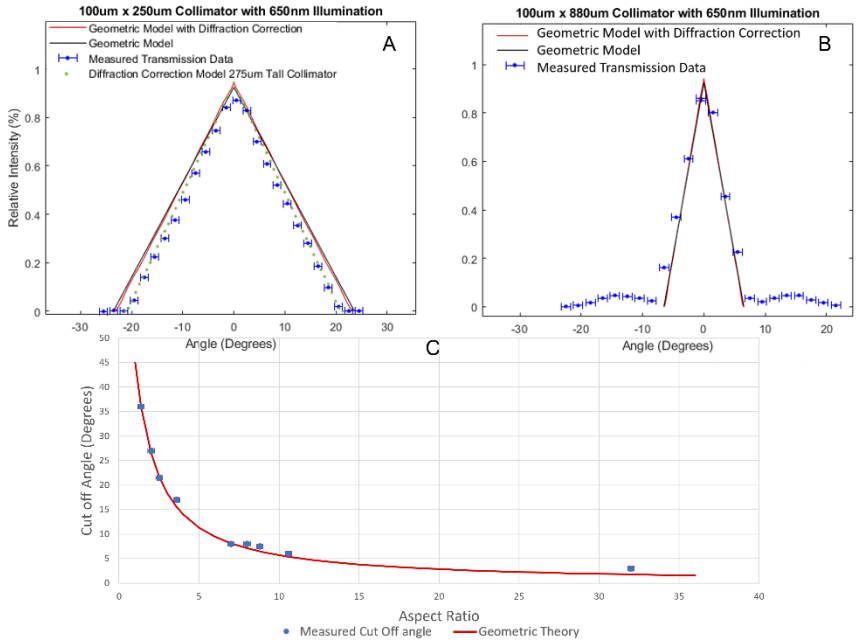

Fig. 3. Collected intensity data vs angle for visible light compared to the model. Shown are data sets collected for two different collimator geometries. A) Transmission through a low aspect ratio (1:2.5) collimator(Pore size: 100 µm, Height: 250 µm) resulting in large angles of light being able to make it through. Because of the uncertainty in the collimator height measurement, an additional model prediction (shown as green dots) for a height of 275 µm is included. B) Transmission through a high-aspect-ratio (1:8.8) collimator(Pore size: 100 µm, Height: 880 µm) resulting in only small angles allowing light to pass. C) Collimation cut off angle vs. collimator aspect ratio. The line shows the prediction from geometric theory shown in Fig. 2 plotted with measured cut off angle values. Aspect ratios range from 1.25 to 32.

Figure 3(b) shows a high-aspect-ratio collimator in comparison to geometric and diffraction corrected models. In addition to the expected linear drop-off of intensity, the high-aspect-ratio collimator exhibited small broad peaks in intensity centered at ± 14 degrees from normal incidence, approximately twice the geometrically expected cut-off angle. We hypothesize that these peaks are due to double reflections off the walls of the infiltrated CNTs pores, which are not as absorbent as as-grown CNTs. Observed intensity must reach the detector on the optic axis of the experiment, eliminating the possibility of single wall reflections and higher order diffraction peaks. Other than at very small angles, light reflected off a single wall (or an odd number of walls) will miss the detector by exiting the collimator at an angle of 2Θ, but light reflecting off two walls (or an even number of walls) will return to the optic axis and be collected. This two-reflection light will be minimum at the critical tilt and maximum at twice the cut-off angle, consequently larger angle two-reflection light will not contribute to the measured intensity below the cut-off angle. We expect that these double reflection peaks to be seen in the low aspect

Optics EXPRESS

ratio data but due to the limited scan range of collimator angles it is not seen in our low aspect ratio data.

Measured cut off angles for collimators with pore sizes of 25, 50, 100, 200 µm and heights from 100 µm to 880 µm are shown in Fig. 3(C) as a function of the aspect ratio with the solid line showing the predicted cut off angle from the geometric model. The collimator cut off value matches closely to that predicted by the geometric model.

The transmission experiments were also performed using collimated IR (1550 nm) light with data shown in Fig. 4 (Dataset 2 Ref. [12]). There were some challenges when working with IR LEDs and InGaAs devices that required some setup modifications. Due to the lower efficiency of IR LEDs the size of the aperture controlling the beam width had to be enlarged to get enough signal to the detector. The area of InGaAs photodetectors is typically much smaller than that of silicon photodetectors, 1 mm x 1 mm for InGaAs but 4.4 mm x 4.4 mm for Silicon. This was compensated for by using an integrating sphere to collect the total signal that passed through the collimator and enters the larger entrance aperture with a 11.4 mm diameter. This larger diameter aperture allows for a even larger portion of the diffraction peaks to be detected, making the diffraction model almost match the geometric model. Figure 4(A) and 4(B) shows the IR

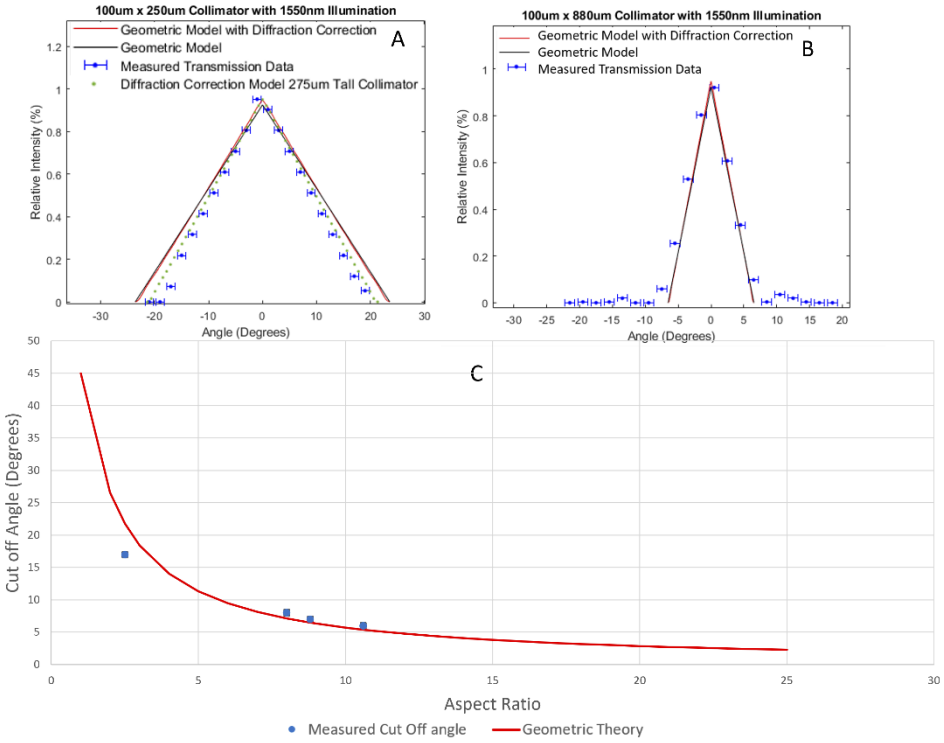

Fig. 4. Data sets of collected intensity data vs angle for IR light compared to the model. Shown are data sets collected for two different collimator geometries. A) A low aspect ratio (1:1.25) collimator resulting in large angles of light being able to make it through. Because of the uncertainty in the collimator height measurement, an additional model prediction (shown as green dots) for a height of 275 µm is included. B) A high aspect ratio (1:8.8) collimator, resulting in only small angles allowing light to pass. C) Collimation cut off angle vs collimator aspect ratio plotted over a similar range as Fig. 3 for easy comparison. The line shows the prediction from geometric theory shown in Fig. 2 plotted with measured cut off angle values. Aspect ratios range from 2 to 10.

Optics EXPRESS

results vs tilt angle for the same collimators as in Fig. 3(A) and 3B. As in Fig. 3, the models shown are not fits to the data but calculations based on the measured or defined geometries of the collimators.

The data is these measurements fit closely to the geometric model due to the large detection area due to the opening of the integrating sphere collecting more of the diffraction peaks. The size of the integrating sphere also brings the detector closer to the collimator, also allowing for more diffraction peaks to be collected. The small double reflection effects are also visible in the high-aspect-ratio IR data. Figure 4(c) shows the measured IR cutoff angles and the predictions of the geometric model. Due to the lower efficiency of IR LEDs the beam size was expanded to allow more light at the detector, this resulted in some of the smaller collimators not being used in for the IR trials, as they were smaller than the beam size. Thus, there are fewer data points in 4C than the corresponding data in 3C.

4. Conclusions

We have demonstrated the effective miniaturization of a collimator based on patterned CNTs. We have shown that with photolithographic patterning we can design a CNT forest in a simple grid pattern. This grid pattern was infiltrated for strength and the resulting material was found to be absorptive of visible and IR light. We showed that this collimator is effective at collimating light in both the visible and near infrared portions of the spectrum. Using a simple geometric model with added far field diffraction effects to calculate transmission we found a correlation between theory and experiment. Although relatively small, double wall reflections were observed. Sidewall reflections of CNT collimators from both one and two walls could be significant to performance in some applications and would be beneficial to study in future work. Improvements to reduce sidewall reflections could involve minimizing infiltration time at the expense of strength/handleability or the use different infiltration materials to maximize absorptivity.

Funding. This research was supported and funded through Tula Health Inc. and Brigham Young University

Acknowledgements. This research was partially supported and funded through Tula Health Inc. We would like to thank the BYU microscopy and cleanroom facilities for their support and help.

Disclosures. T. Westover: Tula Health Inc (F,E,I), Z. Westhoff: Tula Health Inc (F,E), N. Morrill: Tula Health Inc (F,E,I), R. Davis: Tula Health Inc (F,I,P), R. Vanfleet: Tula Health Inc (F,I,P)
S. Olsen declares no conflict exists

Data availability. Data underlying the results presented in this paper are available in Dataset 1 [10], Dataset 2 [12], and Code 1 [11].

References

1. G. H. Chapman, M. S. Tank, G. Chu, and M. Trinh, "In Optical imaging of objects within highly scattering media using silicon-micromachined collimating arrays," in *Optical Fibers and Sensors for Medical Applications II, International Society for Optics and Photonics*: 2002; pp 187–198.
2. M. S. Tank and G. H. Chapman, "Micromachined silicon collimating detector array to view objects in a highly scattering medium," Can. J. Electron. Comp. Eng. **25**(1), 13–18 (2000).
3. Y. Hayamizu, T. Yamada, K. Mizuno, R. C. Davis, D. N. Futaba, M. Yumura, and K. Hata, "Integrated three-dimensional microelectromechanical devices from processable carbon nanotube wafers," Nat. Nanotechnol. **3**(5), 289–294 (2008).
4. G. Chen, B. Dodson, D. M. Hedges, S. C. Steffensen, J. N. Harb, C. Puleo, C. Galligan, J. Ashe, R. R. Vanfleet, and R. C. Davis, "Fabrication of high aspect ratio millimeter-tall free-standing carbon nanotube-based microelectrode arrays," ACS Biomater. Sci. Eng. **4**(5), 1900–1907 (2018).
5. W. C. Fazio, J. M. Lund, T. S. Wood, B. D. Jensen, R. C. Davis, and R. R. Vanfleet, Material Properties of Carbon-Infiltrated Carbon Nanotube-Templated Structures for Microfabrication of Compliant Mechanisms, 2011; *ASMEDC*.
6. B. H. Hanna, W. C. Fazio, J. D. Tanner, J. M. Lund, T. S. Wood, R. C. Davis, R. R. Vanfleet, and B. D. Jensen, "Mechanical Property Measurement of Carbon Infiltrated Carbon Nanotube Structures for Compliant Micromechanisms," J. Microelectromech. Syst. **23**(6), 1330–1339 (2014).
7. S. D. Sypherd, Effects of Infiltration Temperature, Time, and Gas Flow Rate on Material Properties of Carbon Infiltration Carbon Nanotubes. 2019.

Optics EXPRESS

8. D. N. Hutchison, N. B. Morrill, Q. Aten, B. W. Turner, B. D. Jensen, L. L. Howell, R. R. Vanfleet, and R. C. Davis, "Carbon Nanotubes as a Framework for High-Aspect-Ratio MEMS Fabrication," J. Microelectromech. Syst. **19**(1), 75–82 (2010).
9. W. C. Fazio, J. M. Lund, T. S. Wood, B. D. Jensen, R. C. Davis, and R. R. Vanfleet, "Material properties of carbon-infiltrated carbon nanotube-templated structures for microfabrication of compliant mechanisms," *ASME International Mechanical Engineering Congress and Exposition*, 481–490 (2011).
10. T. Westover, "Data collected using a red LED," figshare (2022) [retrieved 2 June 2022], https://doi.org/10.6084/m9.figshare.19706278.
11. T. Westover, "Visible and short-wavelength infrared light collimation through carbon nanotube, parallel-hole collimators," figshare (2022), https://doi.org/10.6084/m9.figshare.19706284
12. T. Westover, "All the data collected for the IR testing," figshare (2022) [retrieved 2 June 2022], https://doi.org/10.6084/m9.figshare.19706263.